PROCEEDINGS, 51st Workshop on Geothermal Reservoir Engineering
Stanford University, Stanford, California, February 9-11, 2026
SGP-TR-230

Numerical Study of Hydraulic Stimulations at the Utah-FORGE Geothermal Site with Coupled THM+E Simulations

Fan Fei[1], Kayla A. Kroll[1], Chaoyi Wang[1], Matteo Cusini[1], Megan Smith[1], Jeffrey Burghardt[2], Luke Frash[3], Chris Marone[4] and Raphael Affinito[4]

[1]Lawrence Livermore National Laboratory, CA, USA

[2]Pacific Northwest National Laboratory, WA, USA

[3]Los Alamos National Laboratory, NM, USA

[4]Pennsylvania State University, PA, USA

E-mail address: fei2@llnl.gov

Keywords: Utah FORGE, Hydraulic Stimulation, Thermo-hydro-mechanical plus Earthquake (THM+E) Modeling, Induced Seismicity

ABSTRACT

The Utah FORGE (Frontier Observatory for Research in Geothermal Energy) project, a U.S. Department of Energy initiative located near Milford, Utah, aims to advance EGS technology. In April 2024, eight new stimulation stages (Stages 3R–10) were conducted in well 16A, following the initial stimulation series (Stages 1–3) in April 2022. Microseismic catalogs and fiber optic data reveal that the fractures stimulated in Stages 3R–6 closely align with that initially generated during Stage 3, suggesting reactivation of existing fractures rather than creation of new fractures in this recent stimulation campaign. To investigate this hypothesis, we adopt a coupled thermo-hydro-mechanical and earthquake (THM+E) simulation workflow to analyze the stimulation activity in well 16(A)78-32, with the primary objective to confirm whether Stages 3R–6 reactivated fractures initially formed in Stage 3. The workflow comprises two sequential modeling steps. Specifically, the first step involves a continuum-based fully coupled THM simulation that incorporates an upscaled permeability field to represent discrete fracture networks. The THM simulation outputs are then post-processed and transferred to an earthquake simulator to model the induced seismic events. Numerical results have illustrated acceptable agreement with the field injection pressure for each stage, when the THM modeling setup includes previously stimulated fracture in the simulation of subsequent stages. Additionally, the full THM+E simulations were conducted, with the purpose to compare the seismic catalog with the field observation. The simulation results have demonstrated a moveout pattern of seismic events away from the injection point through Stages 3–5, showing quantitative similarity to the field observation. Conclusively, these coupled simulation results support the hypothesis that the recent stimulation stages may not generate new fractures, but instead reactivated the same fracture formed in the previous Stage 3 stimulation.

1. INTRODUCTION

The development of enhanced geothermal systems (EGS) primarily consists of hydraulic stimulation and subsequent fluid circulation, both of which involve injection of cold fluid (e.g., water) into hot, dry rock formations. These injection activities can elevate pore pressure, reduce formation temperature, and alter the *in situ* stress state, consequently triggering seismic events. Therefore, a coupled thermo-hydro-mechanical (THM) numerical workflow that is capable of modeling seismic slip is essential for effective EGS development. By integrating key physical processes, this workflow enables accurate simulation of pressure and temperature evolution, stress changes, and induced seismicity, thereby providing a critical tool for induced seismic risk assessment and for optimizing reservoir stimulation and production strategies.

The Utah FORGE project near Milford, Utah, is a U.S. Department of Energy initiative focused on advancing enhanced geothermal system (EGS) technology. Following an initial stimulation campaign (Stages 1–3) conducted in April 2022, a second campaign consisting of eight stimulation stages (Stages 3R[1]–10) was carried out in April 2024 in injection well 16(A)78-32. Induced seismicity during these operations was monitored using a combination of surface geophone patches (Niemz et al., 2025) and downhole geophones deployed in wells 58-32, 56-32, and 78B-32 (Dyer et al., 2023). In addition, fiber optic cables installed in wells 16(B)78-32, 78-32, and 78B-32 were used to complement microseismic data and detect fracture hits.

Analyses of the field datasets have enabled detailed characterization of the stimulation response at the FORGE site. Niemz et al. (2025), for example, identified at least two distinct fracture groups connecting the injection and production wells. Notably, the first fracture group, primarily associated with Stages 3R–6 and partially Stage 7, generally overlaps with the region activated during Stage 3 of the 2022 campaign. Evidence from fiber-optic measurements further supports this interpretation: distributed strain sensing (DSS) data from well 16(B)78-32 show a continuous strain response at a consistent measured depth across Stages 3R–7 (Jurick et al., 2025), suggesting activation of a single fracture zone throughout these stimulation stages. Together, these observations highlight the need for a clear

[1] Stage 3R is a re-stimulation stage of Stages 1–3 in the previous 2022 campaign.

understanding of the coupled THM and earthquake responses so as to better interpret reservoir behavior during and after the stimulation activities.

In this study, we introduce and apply a coupled thermo–hydro–mechanical and earthquake (THM+E) simulation workflow to investigate stimulation activities in well 16(A)78-32. The primary objective is to explore whether Stages 3R–5 reactivated the preexisting fracture zone that was initially formed during Stage 3. To this end, we conduct THM+E simulations for Stages 3, 3R, 4, and 5 individually, incorporating the discrete fracture networks (DFNs) constructed using a plane-fitting technique based on the microseismic catalogs. The simulation workflow consists of two separate numerical models, namely, a THM model and an earthquake model, coupled in a one-way manner. Key simulation results, including injection pressure, permeability evolution, and predicted seismic catalogs, are compared with field observations to validate the modeling workflow and to provide insight into subsurface processes that are not readily accessible through direct field measurements.

The paper is structured as follows. In Section 2, we present detailed analyses of the field data and propose the hypothesis that the new stimulation stages (Stages 3R–6) were probably reactivating the previously stimulated fractures in Stage 3. In Section 3, we introduce the coupled THM+E workflow and the problem setup to validate our hypothesis, followed by the simulation results for each stage in Section 4. Meanwhile, discussions are included to analyze the model predictions and their comparison with field data. Finally, we conclude this numerical investigation and outline future plans in Section 5.

2. ANALYSIS OF UTAH FORGE STIMULATION DATA

In this section, we present and analyze the field data from stimulation activities conducted on well 16(A)78-32, with a focus on the available microseismic and fiber optic data. The analysis implies that the new stimulation stages (Stages 3R–6) were probably *reactivating* the previously stimulated fractures in Stage 3, rather than creating new ones. Details of the analysis are provided below.

2.1 Microseismic Data Analysis

We begin with analysis of microseismic data acquired from both surface and downhole networks of geophones as well as distributed acoustic sensing (DAS) fibers installed along a set of monitoring wells (e.g., 56-32, 78B-32) and the deviated production well 16(B)78-32 (Dyer et al., 2023). Figure 1(a) shows the spatial distribution of all visually checked events from Stages 3R-10 relative to the 16(A)78-32 well, together with events recorded during Stage 3 in 2022. To characterize the locations and orientations of stimulated fractures, we use principal component analysis (PCA) technique to perform plane-fitting for each stimulation stage. PCA is a standard technique used to perform unsupervised clustering for data. Basically, the method identifies the direction where the data have the most spatial variance and fits a plane to that direction. Details of the PCA technique are well documented in other literature (Chopra et al., 2019; Roden et al., 2015) and are omitted here for brevity. The resulting fitted fracture planes for Stages 3-6 are shown in Figure 1(b). As can be seen, the results indicate that the fracture planes for Stages 3-6 are closely aligned. This observation implies the possibility that Stages 3 to 6 stimulated the same fracture or a fractured zone. This interpretation is consistent with observations reported by Niemz et al. (2025) based on microseismic monitoring using (near-)surface geophone networks.

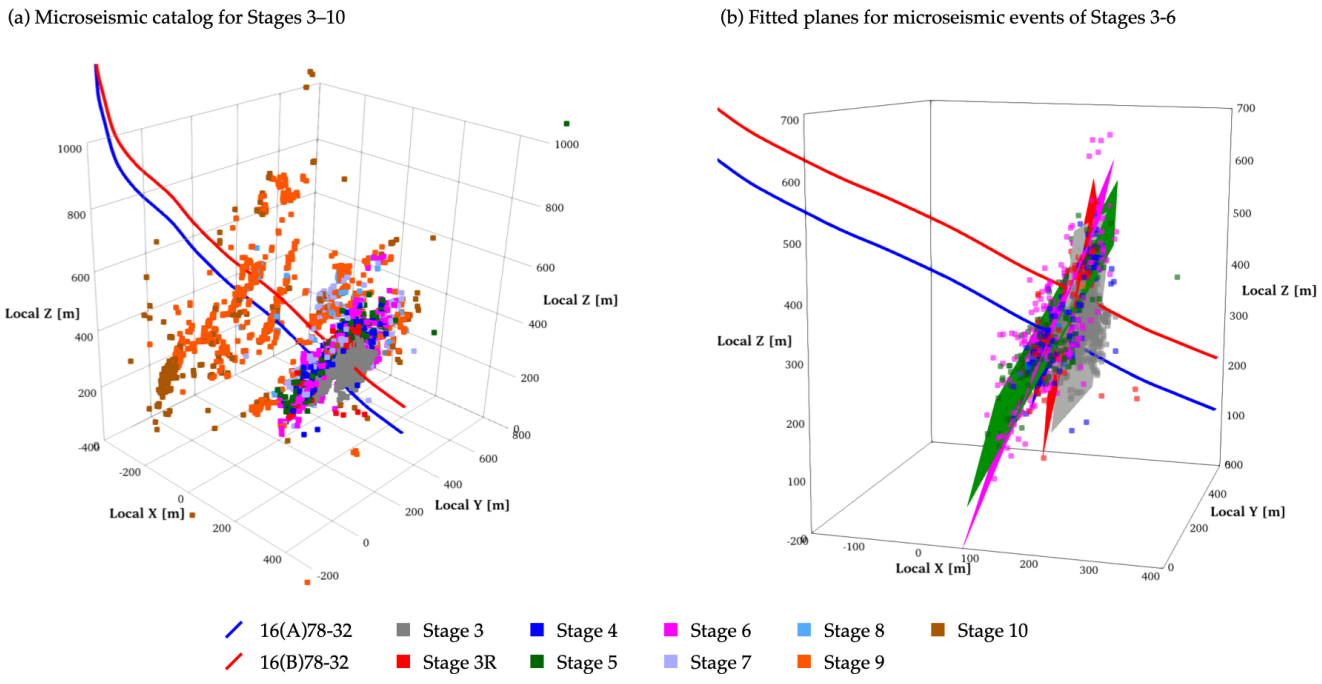

Figure 1 Microseismic catalog for new stimulation stages: (a) spatial distribution of events for Stage 3-10; (b) fitted planes for microseismic events of Stages 3-6.

For further analysis, we pot the microseismic catalogs of Stages 3–6 on a distance-time or radius-time (RT) graph in Figure 2. The RT graph provides visual estimates of how fast the fluid pressure front moves away from the stimulation location. In Figure 2, Stage 3 microseismic (gray circles) events clearly show a gradual increase in distance from the origin over time. This move-out pattern matches the expected microseismic behavior of a propagating fracture. Stage 3R and beyond happened one year later than Stage 3. Therefore, for better visualization, we plot the microseismic events from Stages 3R–6 right after Stage 3. For Stages 3R–6, the move out patterns are not clearly observed as some microseismic events far from the injection occur almost at the same time with the closer events. This observation suggests that Stages 3R–6 were reactivating a preexisting fracture, possibly the one generated during Stage 3, so that the pressure front can travel instantaneously to the edge for these subsequent stages.

To determine whether Stages 3R–6 were stimulating the fracture zone created in earlier Stage 3, we fitted a RT curve for all microseismic events from Stage 3–6 (solid curve in Figure 2) using a volumetric expansion formulation for stimulated fractures (Haffener et al., 2022). The slope of the RT curve generally represents the speed of pressure front. We plot two additional curves representing the scenarios where fluid pressure front moves through the reservoir matrix by diffusion, i.e., the slowest scenario (dashed curve in Figure 2), and that moves through an open fracture by advection, i.e., the fastest scenario (dotted dash curve in Figure 2). The slope of the fitted RT curve lies between the fracture matrix diffusion curve and the advection curve, suggesting the occurrence of a continuously propagating fracture. Furthermore, the microseismic events from Stages 3R–6 are capped by the same RT curve, implying they all originated from the same fracture plane or fracture zone (Kroll et al., 2017).

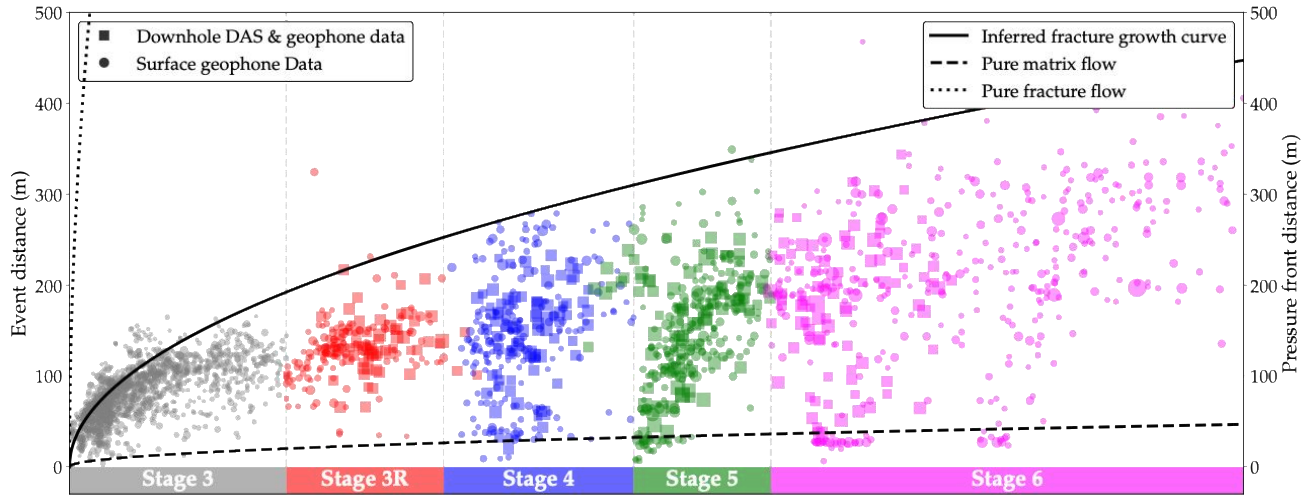

Figure 2 Distance/Radius-time plot for microseismic events of Stages 3-6 using both downhole geophone and DAS data (marked by square) and surface geophone data (marked by circle). The marker is scaled by the event magnitude. The solid curve represents the move-out speed of the events from all stages, along with two additional pressure diffusion curves for the flows in matrix (dashed) and fracture (dotted), respectively. Note that the time axis is not scaled to real time. Events of all stages are combined by linking the last event of one stage to the first event of the next.

2.2 Fiber Optic Data Analysis

The fiber optic data collected during the stimulation also supports the hypothesis. Our analysis here focuses on the distributed strain sensing (DSS) data recorded by the fiber cable installed behind the casing on well 16(B)78-32 (~300 feet above 16(A)78-32), with the goal to identify potential “frac hits”' by examining localized strain changes in response to stimulation. Figure 3 shows a waterfall plot of the strain change along the fiber optic cable during new stimulation stages in 2024 (Jurick et al., 2025). A prominent red strip is clearly visible around 9800 feet MD immediately after Stage 3R begins. Typically, a new fracture will show a red heart-shaped pattern on the waterfall plot when interacting with the fiber optic cable (Jin & Roy, 2017; Wang et al., 2023), because of an advancing "process zone" for a propagating fracture. A strip without apparent heart-shaped pattern indicates the re-opening of an existing fracture (Haffener et al., 2022). Also notably, the red strip signal persists throughout Stages 3R–6 at the same location. No additional signals were observed during the same stimulation period. Diffusive red patterns also appear below the main signal close to the end of Stage 4, but the main signal initiated in Stage 3R remains the dominant feature. The data interpretation provides strong evidence that Stages 3R–6 reopened the same fracture plane around 9800 feet MD of the 16(B)78-32 Well, which supports the hypothesis in the previous section.

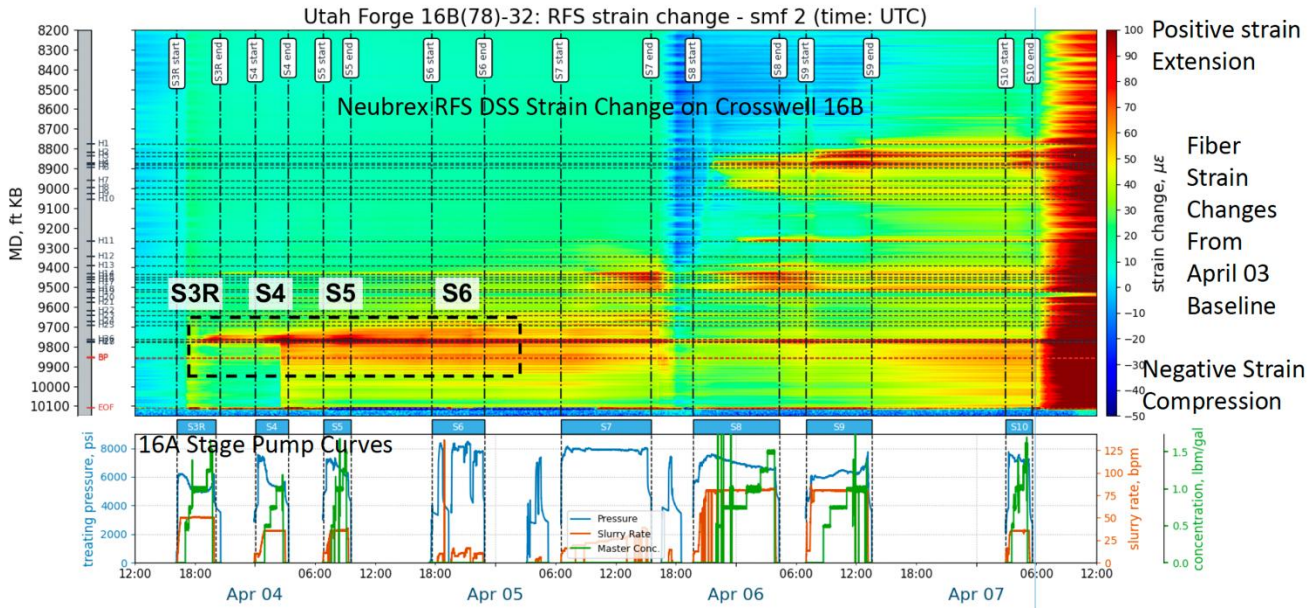

Figure 3 RFS DSS strain change from the fiber optic cable installed on well 16B(78)-32. The figure is directly captured from Jurick et al. (2025) with slight modification.

2.3 Summary of Field Data Analysis

To summarize the field observations discussed above, two hypotheses are proposed based on analyses of microseismic and fiber-optic measurements:

Hypothesis 1 The new stimulation stages 3R-6 were reopening and extending a preexisting fracture zone instead of creating new fractures.

Hypothesis 2 The re-stimulated preexisting fracture zone is possibly the one that was originally generated during Stage 3 stimulation in 2022.

Similar observations and interpretations have been reported within the FORGE community. Several potential mechanisms have been proposed to explain this unexpected stimulation behavior, including possible packer failure and interactions with the natural fracture network. However, to the best of our knowledge, few modeling studies have comprehensively tested or validated the above hypotheses. Accordingly, this study seeks to numerically investigate these hypotheses using the proposed high-fidelity coupled THM+E modeling workflow.

3. THM+E MODELING WORKFLOW AND PROBLEM SETUPS

In this section, we demonstrate a coupled THM+E simulation workflow to numerically investigate our hypothesis that Stages 3R–6 were essentially reactivating the previously stimulated region generated during Stage 3, rather than initiating new fractures. The section is structured as follows. First, we introduce the coupled workflow for the THM+E simulation. We then describe THM modeling setup for Stages 3–5, incorporating the DFN permeability field derived from the plane-fitting results shown in Figure 1(b). The problem setup and modeling parameters for the earthquake solver is also provided. Note that Stage 6 is excluded from this study due to unexpectedly high injection pressure obtained in the field.

3.1 Modeling Workflow

The modeling workflow integrates a THM simulation with an earthquake simulation, coupled in a one-way manner through following three steps:

1. **THM simulation:** The workflow begins with a THM simulation using the thermo-poromechanics solver built in GEOS (Settgast et al., 2024), a multiphysics simulator based on the coupled finite element and finite volume method. We use fully implicit THM solver to capture the THM response of the system.
2. **THM results processing:** Upon completion of the THM simulation, we extract the time histories of pressure and effective stress, projecting the data onto the fault planes defined in the subsequent earthquake simulation.
3. **Earthquake simulation**: The stress and pressure data are then transferred to an earthquake simulator based on quasi-dynamic boundary element method, RSQSim (Richards-Dinger & Dieterich, 2012), for conducting earthquake simulations on the fault planes.

We note that a similar one-way coupled workflow has been employed successfully for the THM+E simulation of other EGS projects (Kroll et al., 2021).

3.2 THM Modeling Setup

The THM simulation setup with DFN permeability is presented in Figure 4, including all stages of interest in this study, i.e., Stages 3–5. To validate our hypothesis that new stimulation stages primarily reactivated the region stimulated during Stage 3, we design two problem setups, namely, one for Stage 3 and the other for Stages 3R–5. The only difference between these setups lies in the DFN permeability field. More specifically, the Stage 3 setup includes only those DFNs associated with Stages 1 and 2, whereas the setup of Stages 3R-5 incorporates additional DFNs fitted to microseismic data of new stimulation stages, to align our assumption that these new stimulations were reactivating the pre-existing fractures. Both setups adopt the initial conditions of pressure, temperature, and in situ stresses provided in Table 1. The essential material properties used in the simulations are summarized in Table 2.

To account for permeability enhancement due to hydraulic stimulation, we employ the following pressure-dependent permeability model (Morrow & Lockner, 2012; Nathenson, 1999) to provide a first-order approximation, which has also been utilized by Lee and Ghassemi (2023) in FORGE modeling,

$$\bar{k}(p) = k_0 \exp[\alpha_k (p - p_0)], \tag{1}$$

where α_k is a pressure-dependence coefficient, p_0 indicates the initial pressure. Also, we consider an anisotropic permeability, assuming hydraulic fractures propagate in the direction normal to the x-direction (σ_h), such that permeability enhancement occurs only in *y*- and *z*-directions:

$$\mathrm{k_x} = \mathrm{k_0}, k_y = k_z = \max\{\bar{k}(p), k_{max}\}, \tag{2}$$

where k_{max} denotes a maximum attainable permeability. In the following numerical examples, we calibrate α_k and k_{max} by history matching the observed injection pressure for each stimulation stage.

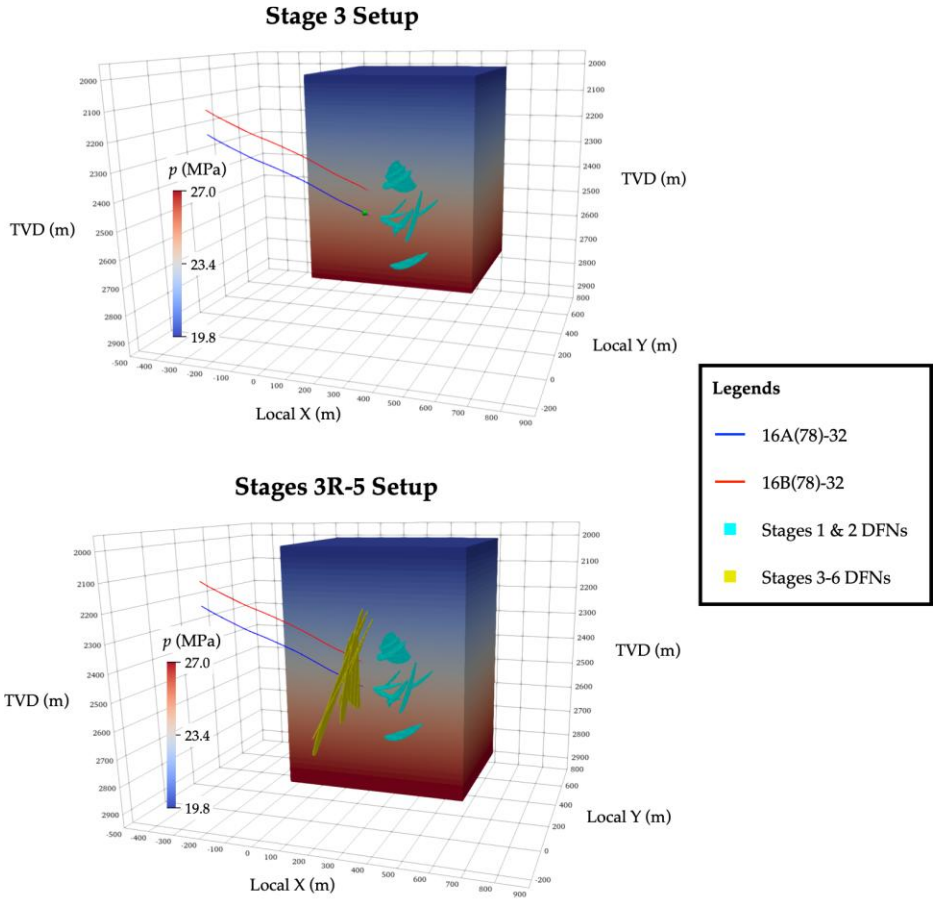

Figure 4 Overview of the THM problem setup with DFN permeability.

Table 1 Initial conditions for the simulation.

Variable	Value at TVD=2775 m	Gradient

Pressure, p	27.04 MPa	0.00981 MPa/m
Temperature, T	194.5 °C	0.06 °C/m
Total minimum horizontal stress, σ_h	46.06 MPa	0.0132 MPa/m
Total maximum horizontal stress, σ_H	52.06 MPa	0.0132 MPa/m
Total vertical stress, σ_v	67.94 MPa	0.0195 MPa/m

Table 2 Material properties adopted in the THM simulation.

Rock matrix	
Elastic modulus, E	55 GPa
Poisson ratio, ν	0.26
Biot coefficient, b	1.0
Reference permeability, k_0	50×10^{-18} m^2
Initial porosity, ϕ_0	0.01
Thermal expansion coefficient, α_T	10^{-7} °C^{-1}
Volumetric heat capacity, C_m	2400 kJ/K/m^3
Thermal conductivity, k_T	4.0 W/K/m
Fluid	
Viscosity, μ_f	0.001 Pa·s
Compressibility, c_w	10^{-8} Pa^{-1}
Specific heat capacity, C_f	4200 J/K/kg
Upscaled DFN permeability	
Initial aperture, ω_0	0.06 mm

3.3 Earthquake Modeling Setup

RSQSim uses a rate- and state-dependent friction (RSF) (Dieterich, 1979; Ruina, 1983) to determine frictional shear resistance, τ^{fric}, whose constitutive relation is formulated as,

$$\tau^{\text{fric}} = (\sigma_N - p)\left[\mu_0 + A\ln\left(\frac{V}{V^*}\right) + B\ln\left(\frac{\theta V^*}{D_c}\right)\right], \tag{3}$$

where A and B are the constitutive parameters that describe the material, D_c is a characteristic slip distance over which the state variable (θ) evolves, μ_0 is the steady-state coefficient of friction at the constant normal stress and the reference slip speed, V^*. The state-variable evolves by the RSF aging law (Linker & Dieterich, 1992) given by

$$\dot{\theta} = 1 - \frac{\theta V}{D_c} - \alpha\left(\frac{\theta\dot{\sigma_{\text{eff}}}}{B\sigma_{\text{eff}}}\right). \tag{4}$$

where α is a dimensionless constant defined below that is typically in the range of 0.25–0.5 (Hong & Marone, 2005; Shreedharan et al., 2019) and σ_{eff} is the effective normal stress,

$$\alpha = \frac{\Delta\tau_\alpha/\sigma_N}{\ln\left(\sigma_N/\sigma_{N,0}\right)} \tag{5}$$

Equation (4) accounts for the perturbation of state due to a change in normal stress and if the change is a Heaviside step the second differential term in Eq. (4) has no effect on the post-step solution scheme because the time derivative of normal stress is zero after the first iteration.

A planar fracture plane is generated at the location of the magenta plane in Figure 1(b) and discretized into 10 m rectangular elements. The slip vector (rake=–156.76º) is computed along this plane (with strike = 171º and dip = 69.78º) by finding the direction of maximum traction along the planar surface in the stress field. Note that because these simulations have been carried out to investigate the hypothesis that the only new fracture to be generated occurred during the Stage 3 stimulation and all other Stages reactivated that same plane, we chose to simulate events along a single plane and do not consider the splay fracture that became activated following Stage 3 stimulation.

All pre-existing conditions and rate-state properties are uniform across the fracture surface, with the exception of the pre-existing shear stress conditions as shown in Figure 5. The shear stress pattern on fractures arises due to heterogeneous crustal properties, geometric complexities along fault and/or fractures, and previous slip events. Here, we use a single stochastic realization based on the von Kármán auto-correlation function (Mai & Beroza, 2002). These types of correlated random fields are described by the power spectral density (PSD) such that,

$$PSD \propto \frac{1}{(1+k^2)^{H+1}}, \tag{6}$$

where k is the dimensionless spatial wavenumber given by $k = \sqrt{{a_x}^2 {k_x}^2 + {a_y}^2 {k_y}^2}$, H is the Hurst exponent, and a_x and a_y define the maximum wavelengths in the x and y direction, respectively. The field used here can be recreated based on the following parameters: H = 0.2, correlation length = 2270 m, standard deviation of the amplitude variation of 4 MPa and random seed value = 12345. All other parameters are listed in Table and are based on lab experiments performed on Utah FORGE rock.

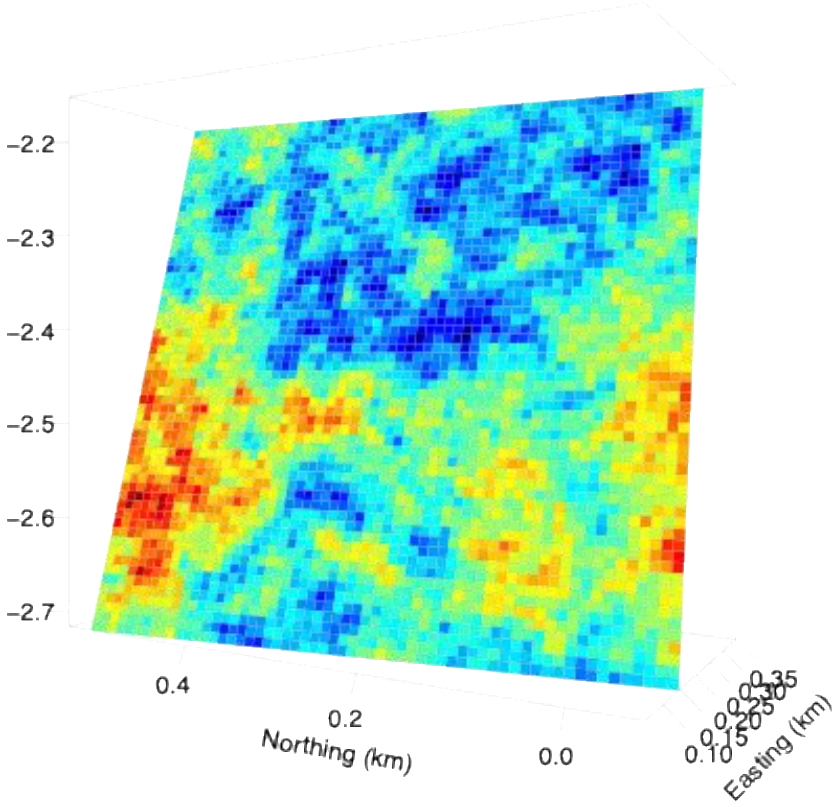

Figure 5 Visualization of the nonuniform pre-existing shear stress field used on the fracture surface at onset of the Stage 3 stimulation. The minimum (blues), maximum (reds), and average values of this distribution are 2.75 MPa, 27.85 MPa, and 14 MPa, respectively.

Table 3 Rate-state properties adopted in the RSQSim earthquake simulation.

RSQSim parameters	**Values**
Rate coefficient, *A*	0.004

Rate coefficient, B	0.00533
Nominal coefficient of friction, μ_0	0.7
Characteristic slip distance, D_c	9×10^{-6} m
Reference velocity, V^*	10^{-6} m/s
Slip velocity, V	1 m/s
Rate-state normal stress dependency, α	0.05
Lamé parameter, λ and G	2400 GPa
Initial normal stress, σ_0	20 MPa
Initial state variable, θ_0	3.15×10^{-7} s

The simulations conducted here neglect the impacts of tectonic loading but do consider the full poroelastic stress and pore-fluid pressure changes. For this coupling, both the dynamic values of the shear and normal stresses in Eq. (3) are provided by the THM simulation and projected onto a fracture surface. The pressure and stress history from all stimulations (Stage 3, 3R, 4, and 5) are concatenated to drive a single continuous simulation that preserves the 2–year time gap between Stage 3 and 3R.

4. THM+E SIMULATION RESULTS AND DISCUSSIONS

Using the THM+E workflow described above, we simulate stimulation activities in well 16(A)78-32 to test two hypotheses in Section 2.3 inferred from field observations. Individual THM simulations are performed for Stages 3–5 using their corresponding DFN-based permeability fields. The resulting pressure and stress fields are then transferred to the earthquake simulator following the workflow outlined in Section 3. A single continuous earthquake simulation is conducted for all stages in chronological order, and the simulated seismic catalogs are compared with field microseismic data to assess the validity of the proposed hypotheses.

4.1 THM Simulations

We present the THM simulation results for Stages 3–5, analyzing each stage individually. It is noted that the simulations for Stages 3R-5 use the bottom setup shown in Figure 4, which incorporates new DFN permeability to represent the stimulated region from Stage 3.

Stage 3. We begin with the THM simulation of Stage 3. Injection pressure history matching is achieved by calibrating the pressure-dependent permeability model with $\alpha_k = 0.8$ MPa^{-1} and $k_{\text{perm},max} = 10^{-7}$ m^2, resulting in good agreement with the observed bottom-hole pressure evolution as shown in Figure 6, including both the peak pressure and subsequent pressure decline. The simulated permeability and pressure fields in Figure 7 show progressive initiation and lateral propagation of the stimulated region during injection due to the prescribed anisotropic permeability in Eq. (2), with pressure diffusion preferentially confined within the fracture plane. Comparison with the microseismic catalog in Figure 8 indicates that the modeled stimulated region closely matches the observed microseismic cloud in both spatial extent and location, supporting the effectiveness of the adopted permeability enhancement model. However, the simulation does not reproduce the upward growth of the stimulated region inferred from microseismic observations, as permeability enhancement in the current model is driven solely by pressure changes. This limitation motivates future incorporation of stress-dependent permeability to better capture the observed stimulation behavior.

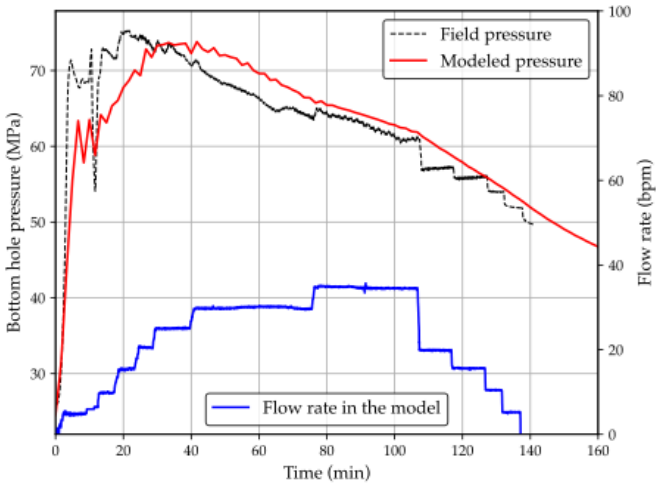

Figure 6 Injection pressure comparison between THM simulation and field data for Stage 3.

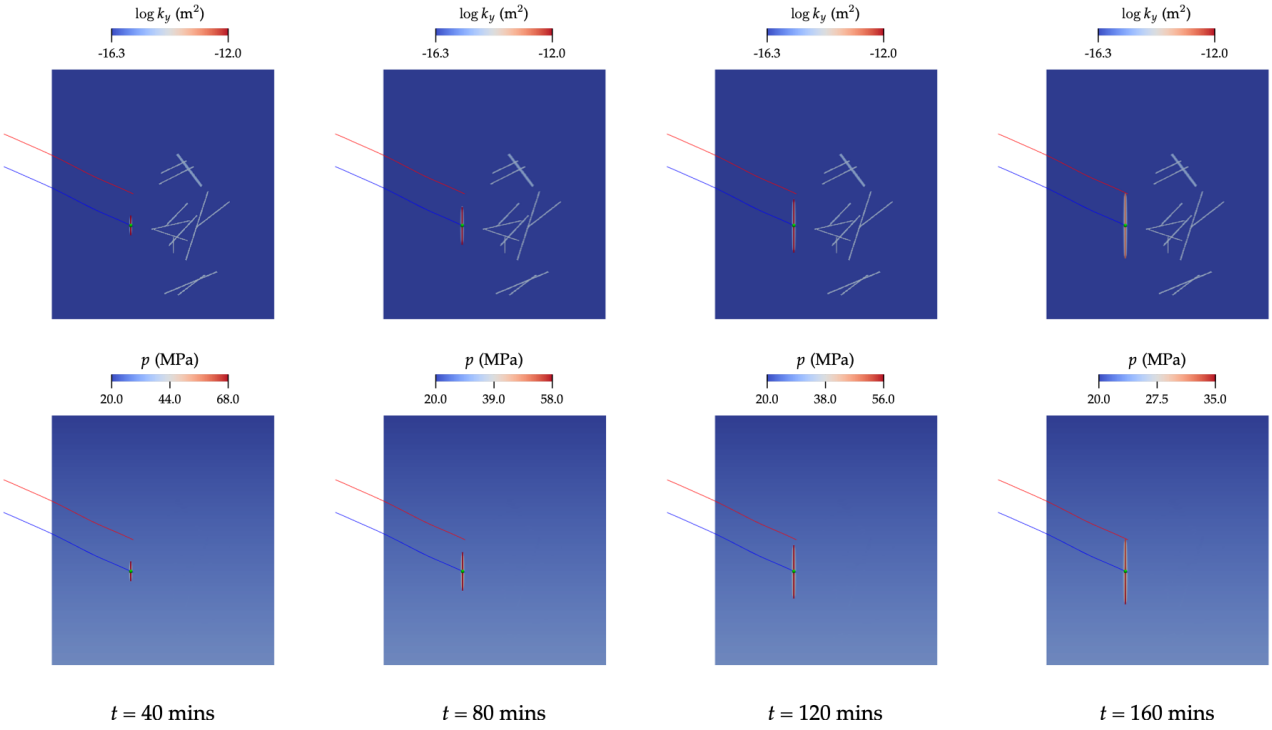

Figure 7 Distribution of permeability (upper row) and pressure (bottom row) for Stage 3 at different stages of injection. Wells 16A and 16B are shown in blue and red, respectively. The injection region is marked as a green circle.

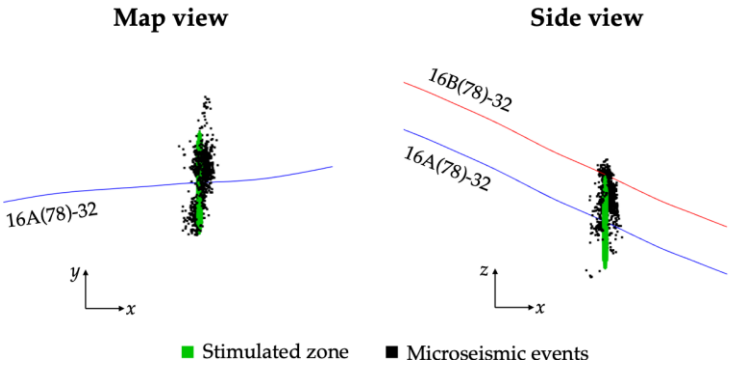

Figure 8 Comparison between the stimulated region from the THM simulation and the spatial distribution of microseismic data for Stage 3.

Stage 3R. The Stage 3R simulation targets re-stimulation of the fracture zone activated during the 2022 campaign. For modeling simplicity, injection is applied at the Stage 3 location only, with the injection rate set to 30% of the total field rate based on flow-partition measurements from the July 2023 circulation test. Injection pressure history matching is achieved using $\alpha_k = 1.2$ MPa^{-1} and $k_{max} = 1.2 \times 10^{-13}$ m^2, producing a pressure response consistent with field observations (Figure 9). Compared to Stage 3, the larger α_k indicates more rapid permeability enhancement, consistent with reopening of preexisting fractures, while the substantially lower maximum permeability is required to reproduce the elevated residual pressure observed in the field. Spatial distributions of pressure and permeability in Figure 10 show that stimulation initiates along the preexisting Stage 3 fracture plane and remains vertically confined throughout injection.

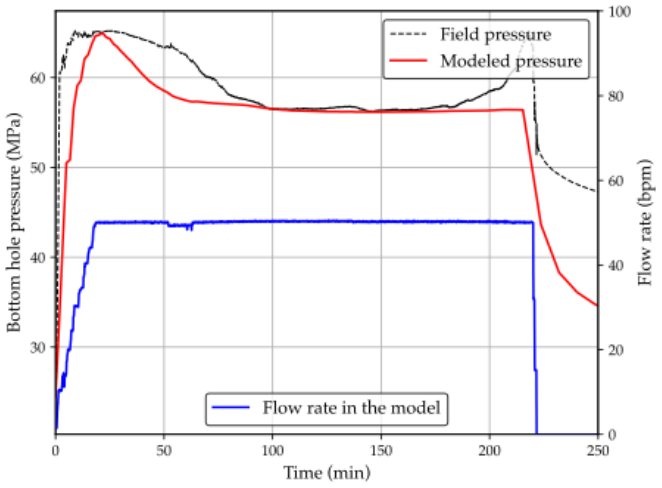

Figure 9 Injection pressure comparison between THM simulation and field data for Stage 3R.

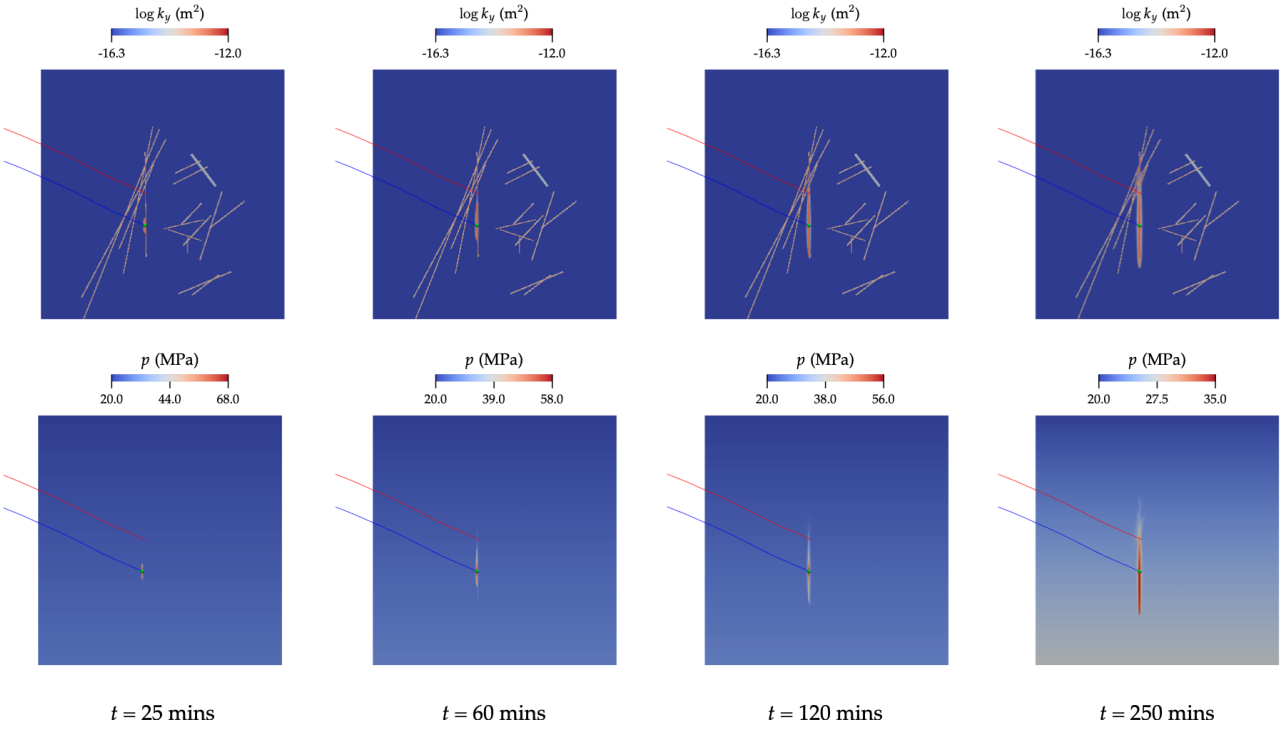

Figure 10 Distribution of permeability (upper row) and pressure (bottom row) for Stage 3R at different stages of injection. Wells 16A and 16B are shown in blue and red, respectively. The injection region is marked as a green circle.

Stage 4. Following the re-stimulation during Stage 3R, the Stage 4 simulation exhibits enhanced hydraulic connectivity and more efficient permeability development. Injection pressure history matching shown in Figure 11 is achieved with $\alpha_k = 3.0$ MPa^{-1} and $k_{\max} = 10^{-12}$ m^2, producing a pressure evolution consistent with the observed pressure decline and residual pressure. The larger calibrated permeability parameters relative to Stages 3 and 3R suggest easier fracture opening, likely facilitated by the short time interval between stages and prior reservoir re-stimulation. Analysis of the pressure and permeability fields in Figure 12 shows that the stimulated region expands with injection and intersects preexisting DFNs approximately 40–60 minutes into the stage, coinciding with the onset of pressure drop. As injection progresses, pressure diffusion branches and connects with the fracture planes associated with Stages 3 and 3R, indicating hydraulic communication between stages and supporting fracture reactivation rather than the creation of new isolated fractures.

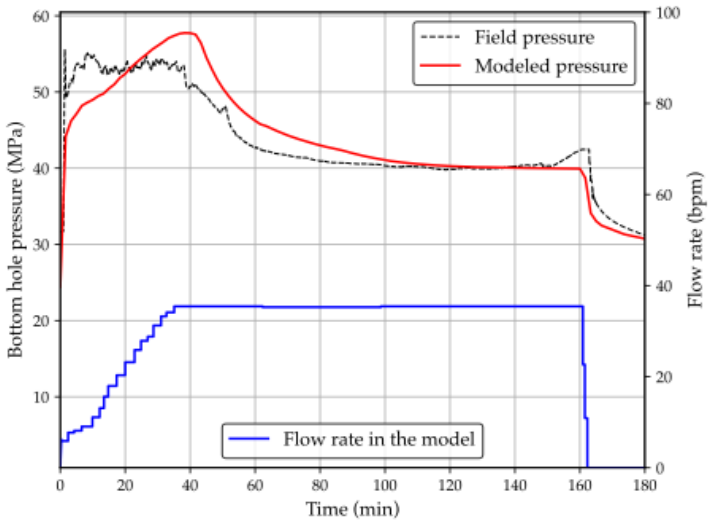

Figure 11 Injection pressure comparison between THM simulation and field data for Stage 4.

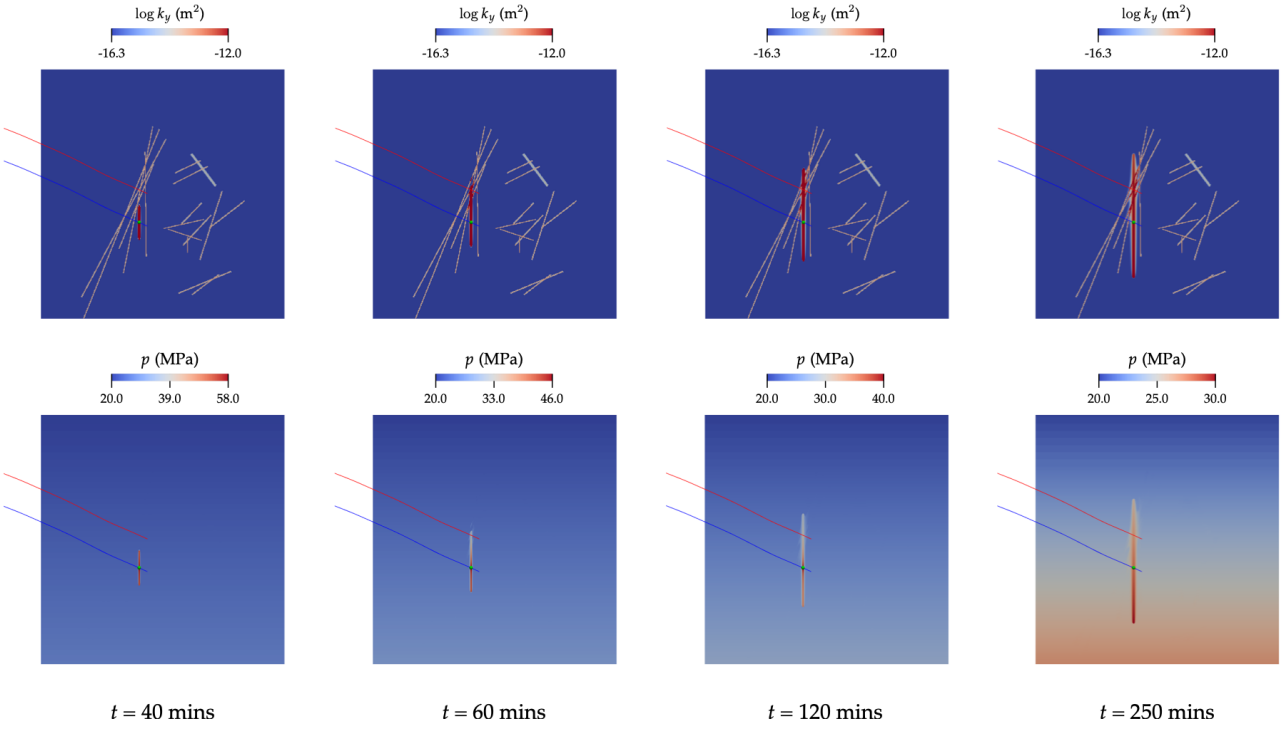

Figure 12 Distribution of permeability (upper row) and pressure (bottom row) for Stage 4 at different stages of injection. Wells 16A and 16B are shown in blue and red, respectively. The injection region is marked as a green circle.

Stage 5. The Stage 5 simulation exhibits slower pressure dissipation and more limited permeability enhancement compared to Stages 3R and 4. Injection pressure history matching is achieved using $\alpha_k = 0.6$ MPa^{-1} and $k_{\max} = 10^{-12}$ m^2, reproducing the observed gradual pressure decline as shown in Figure 13. The smaller calibrated α_k value indicates reduced permeability enhancement, which may be attributed to the use of high-viscosity crosslinked gel or to stress shadowing effects that constrain fracture opening. In contrast to earlier stages, Stage 5 also exhibits a lower peak injection pressure, suggesting early hydraulic connection with preexisting fracture networks. This interpretation is supported by the pressure and permeability fields as presented in Figure 14, which show intersection between the stimulated region and preexisting DFNs within the first 10 minutes of injection. The rapid establishment of connectivity provides additional flow pathways and limits pressure buildup, consistent with reactivation of previously stimulated fractures rather than the formation of new fracture zones.

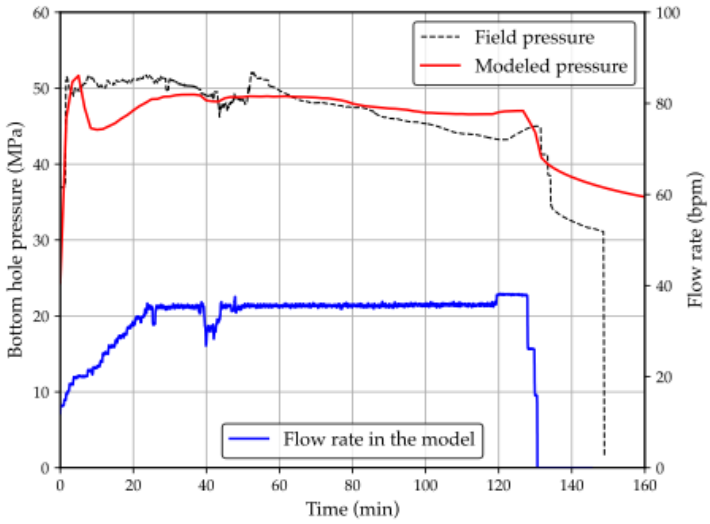

Figure 13 Injection pressure comparison between THM simulation and field data for Stage 5.

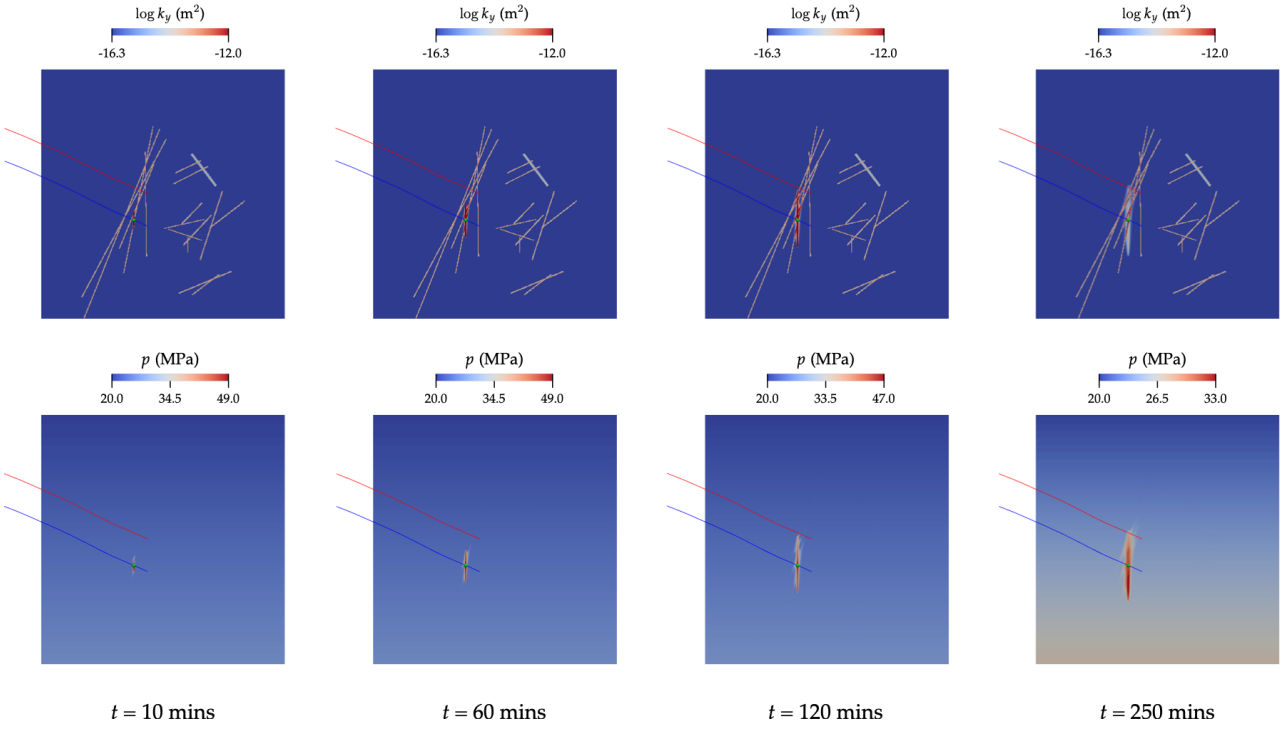

Figure 14 Distribution of permeability (upper row) and pressure (bottom row) for Stage 5 at different stages of injection. Wells 16A and 16B are shown in blue and red, respectively. The injection region is marked as a green circle.

4.2 Coupled THM+E Simulations

The pressure and stress histories from all stimulation stages (Stages 3, 3R, 4, and 5) are concatenated and used to drive a single earthquake simulation that spans all stages and preserves the time delay between Stages 3 and 3R. Because the earthquake simulations are deterministic and the spatial and temporal patterns of seismicity emerge from complex interactions among injection-induced stress changes, coseismic slip, material properties, and frictional behavior, it is impossible to predict the exact timing and location of individual seismic events as observed in the field. As a result, traditional history-matching approaches commonly used in reservoir simulation are not applicable. Instead of attempting to match the time history or spatial evolution of individual events, we evaluate model performance by comparing catalog-level properties, including event rates, magnitude distributions, and the spatiotemporal evolution of seismicity.

Figure 15 compares the cumulative number of simulated events with those observed in the field for each stimulation stage. Event magnitudes are reported for $M \geq -1.5$ for Stage 3 and $M \geq 0$ for the remaining stages. The cutoff for Stage 3 reflects the magnitude of completeness of its microseismic catalog, whereas for the latter stages (Stages 3R–5), the field data presented here are solely from

downhole monitoring, for which only events with M ≥ 0 were reviewed and included. For Stage 3, the analysis is further restricted to events occurring within the first 300 minutes after the start of injection. This is because the simulation considers only a single fracture plane and does not include the secondary splay fracture that becomes active over 400 minutes after Stage 3 stimulation. Overall, the simulations well capture the onset timing of seismic events and the general event rates for Stages 3, 4, and 5. Notably, the simulations for Stages 4 and 5 tend to generate a larger total number of events than observed, whereas relatively few events are produced during the Stage 3R simulation.

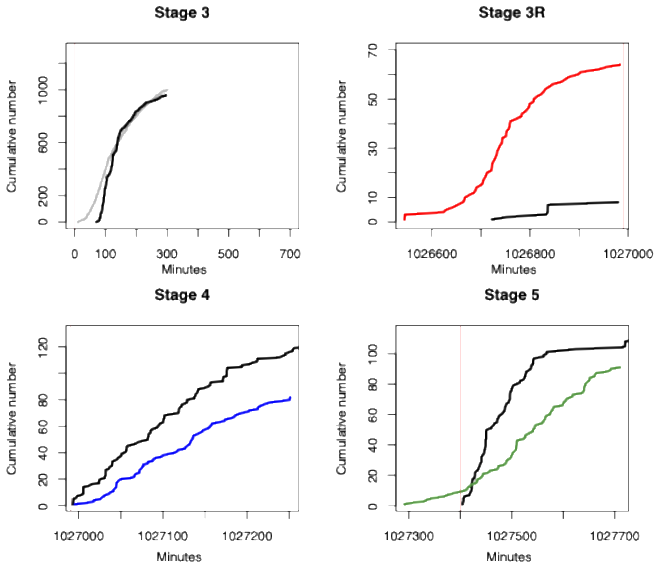

Figure 15 Comparison of the cumulative number of events that occur in the simulation (black) and the observed number of events that occur in the field during each stimulation.

Figure 16 compares the spatial distributions of simulated and observed seismic events, colored by stimulation stage, from three orthogonal viewing directions. In both the simulations and observations, events tend to be clustered by stage, but generally migrate in similar directions, indicating potential reactivation of the preexisting fracture zone by subsequent stimulation stages.

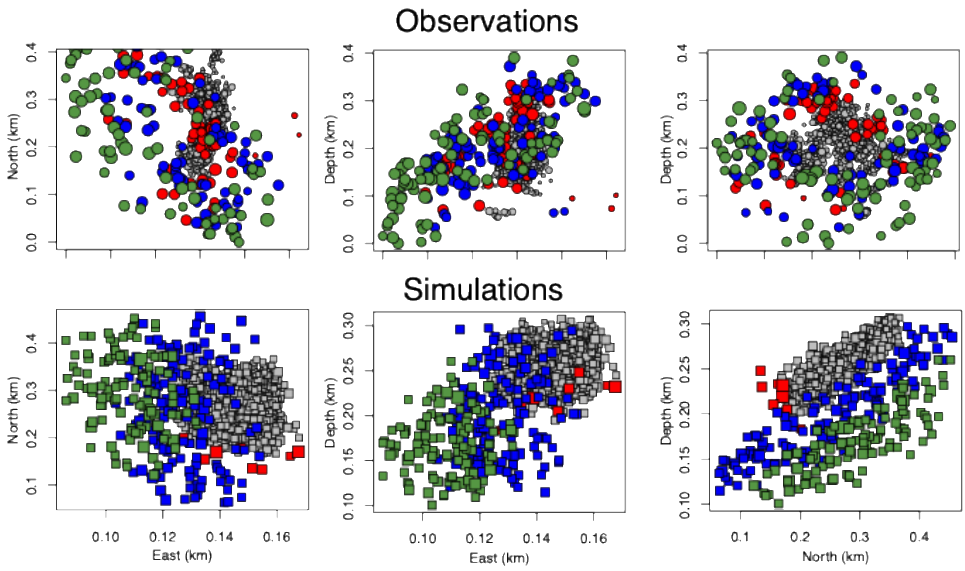

Figure 16 Comparison of spatial distribution of observed events (top row) and the simulated events (bottom row). The color indicates the stage the events are associated with: Stage 3 (grey), Stage 3R (red), Stage 4 (blue), Stage 5 (green).

To further investigate the spatiotemporal evolution of seismic activity, Figure 17 shows the distance between each event and the corresponding injection location as a function of time, with the time gap between Stage 3 and Stage 3R removed for clarity. The simulated event migration exhibits good agreement with that inferred from the observed microseismic data. Moreover, we also plot three diffusion curves to illustrate the expected moveout of events if the seismic activity is being induced by three flow regimes: pure matrix flow (dashed

and dotted line), pure fracture flow (dashed line), and the fitted envelop based on the field data representing flow in a growing fracture into rock matrix (solid line). If the seismic events are controlled by pure matrix flow, this would imply that no fracture is generated and that fluids are migrating primarily through the rock pore space. Conversely, if the observed seismicity follows the pattern indicated by pure fracture flow, that would suggest the presence of an already sustained/propped, relatively large-aperture fracture. As we can see, neither pure matrix flow curve nor pure fracture flow curve seems to explain the moveout pattern of observed seismic events for all stages. Instead, the event moveout is best explained by the intermediate solid curve, which is consistent with a scenario in which previously generated fractures have experienced partial closure, maintaining small apertures with asperity contact while still allowing further fracture extension and fluid flow through both fractures and surrounding matrix. This behavior is observed in both the simulated and field seismic catalogs and is consistent with the hypothesis of fracture reactivation rather than the creation of entirely new fracture systems.

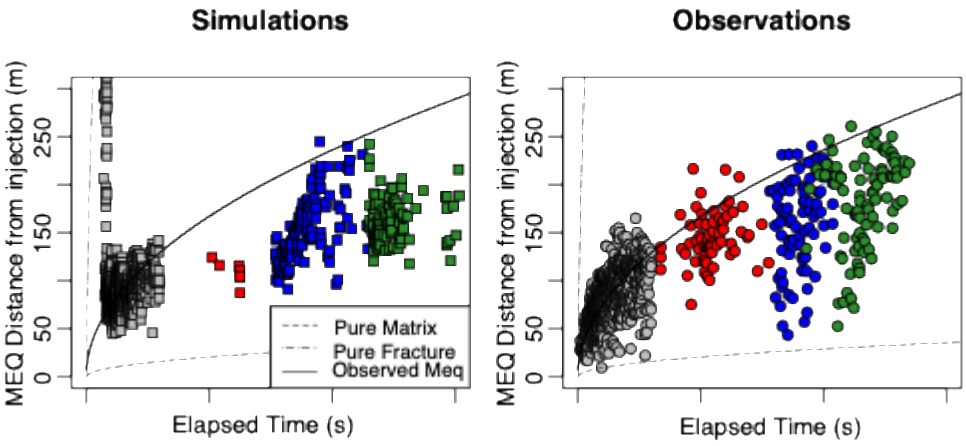

Figure 17 Comparison of the distance between each event and the injection point for the simulation events (left) and observed events (right) with color representing the stage (as in Figure 16). Curves show the projected moveout of seismic events away from the injection point in time, assuming three flow regimes: pure matrix flow (dashed and dotted line), pure fracture flow (dashed line), and the fitted envelop based on the field data representing flow in a growing fracture into rock matrix(solid line).

CONCLUSIONS

In this work, we have proposed and applied a coupled THM+E modeling workflow to simulate recent stimulation activity at the Utah FORGE site and to evaluate two hypotheses regarding fracture generation and reactivation during stimulation Stages 3, 3R, 4, and 5. The results of the THM+E simulation with only a single fault plane show acceptable agreement with the field observation, which provides strong support that the later stimulation stages (3R–5) were primarily reopening and extending a unique preexisting fracture rather than generating new fractures (*Hypothesis 1*). In addition, the "frac hits" detected by the DSS data and the moveout pattern of seismic events shown in both observation and our simulations indicate that this preexisting, re-stimulated fracture zone corresponds to the fracture initially generated during the Stage 3 stimulation (*Hypothesis 2*). We note that if the alternative interpretation is correct, namely, that each stimulation stage generated an independent fracture, such agreement between the simulated responses and the observed data would not be expected.

Despite the overall consistency, some discrepancies remain, particularly the limited seismic events produced during the Stage 3R simulation. This behavior may reflect some limitations in the assumed initial stress conditions. In fact, the Stage 3 stimulation produces seismic events at relatively large distances from the injection point, which are more likely influenced by stress interactions than by direct pore-pressure perturbations. This observation suggests that the initial shear stress state may be too high in the current model. Further refinement of the initial stress conditions and associated model parameters is in progress based on systematic parametric studies.

ACKNOWLEDGEMENTS

This work was performed under the auspices of the U.S. Department of Energy by Lawrence Livermore National Laboratory under Contract DE-AC52-07NA27344.

REFERENCES

Chopra, S., Marfurt, K., & Sharma, R. (2019). Unsupervised machine learning facies classification in the Delaware Basin and its comparison with supervised Bayesian facies classification. SEG International Exposition and Annual Meeting, San Antonio, Texas, USA.

Dieterich, J. H. (1979). Modeling of rock friction: 1. Experimental results and constitutive equations. *Journal of Geophysical Research: Solid Earth*, *84*(B5), 2161-2168. https://doi.org/10.1029/JB084iB05p02161

Dyer, B., Karvounis, D., & Bethmann, F. (2023). Microseismic event catalogues from the well 16A(78)-32 stimulation in April, 2022 in Utah FORGE. *ISC Seismological Dataset Repository*. https://doi.org/https://doi.org/10.31905/52CC4QZB

Haffener, J., Haustveit, K., & Trevor, I. (2022). Did We Break New Rock? Utilizing Diagnostics to Differentiate New Fracture Creation vs Old Fracture Reactivation: A Meramec and Wolfcamp Study. SPE Hydraulic Fracturing Technology Conference and Exhibition, The Woodlands, Texas, USA.

Hong, T., & Marone, C. (2005). Effects of normal stress perturbations on the frictional properties of simulated faults. *Geochemistry, Geophysics, Geosystems*, *6*(3). https://doi.org/10.1029/2004gc000821

Jin, G., & Roy, B. (2017). Hydraulic-fracture geometry characterization using low-frequency DAS signal. *The Leading Edge*, *36*(12), 975-980. https://doi.org/10.1190/tle36120975.1

Jurick, D., Reynolds, A., & Sharma, M. M. (2025). Improving the Connectivity Between Injection and Production Wells in Enhanced Geothermal Systems Using Fiber Optic Data. *SPE Hydraulic Fracturing Technology Conference and Exhibition*.

Kroll, K. A., Richards-Dinger, K. B., & Dieterich, J. H. (2017). Sensitivity of Induced Seismic Sequences to Rate-and-State Frictional Processes. *Journal of Geophysical Research: Solid Earth*, *122*(12). https://doi.org/10.1002/2017jb014841

Kroll, K. A., Wu, H., & Fu, P. (2021). *Exploring Whether Subsurface Fluid Production Can Minimize Triggered Seismicity in Geothermal Fields*.

Lee, S. H., & Ghassemi, A. (2023). Modeling and Analysis of Stimulation and Fluid Flow in the Utah FORGE Reservoir. 48th Workshop on Geothermal Reservoir Engineering, Stanford University, Stanford, California, USA.

Linker, M. F., & Dieterich, J. H. (1992). Effects of variable normal stress on rock friction: Observations and constitutive equations. *Journal of Geophysical Research: Solid Earth*, *97*(B4), 4923-4940. https://doi.org/10.1029/92jb00017

Mai, P. M., & Beroza, G. C. (2002). A spatial random field model to characterize complexity in earthquake slip. *Journal of Geophysical Research: Solid Earth*, *107*(B11). https://doi.org/10.1029/2001jb000588

Morrow, C. A., & Lockner, D. A. (2012). Permeability differences between surface-derived and deep drillhole core samples. *Geophysical Research Letters*, *21*(19), 2151-2154. https://doi.org/10.1029/94gl01936

Nathenson, M. (1999). The dependence of permeability on effective stress from flow tests at hot dry rock reservoirs at Rosemanowes (Cornwall) and Fenton Hill (New Mexico). *Geothermics*, *28*(3), 315--340.

Niemz, P., Pankow, K., Isken, M. P., Whidden, K., McLennan, J., & Moore, J. (2025). Mapping Fracture Zones with Nodal Geophone Patches: Insights from Induced Microseismicity During the 2024 Stimulations at Utah FORGE. *Seismological Research Letters*, *96*(3), 1603-1618. https://doi.org/10.1785/0220240300

Richards-Dinger, K., & Dieterich, J. H. (2012). RSQSim Earthquake Simulator. *Seismological Research Letters*, *83*(6), 983-990. https://doi.org/10.1785/0220120105

Roden, R., Smith, T., & Deborah, S. (2015). Geologic pattern recognition from seismic attributes: Principal component analysis and self-organizing maps. *Interpretation*, *3*(4), 59-83.

Ruina, A. (1983). Slip instability and state variable friction laws. *Journal of Geophysical Research: Solid Earth*, *88*(B12), 10359-10370. https://doi.org/10.1029/JB088iB12p10359

Settgast, R. R., Aronson, R. M., Besset, J. R., Borio, A., Bui, Q. M., Byer, T. J., Castelletto, N., Citrain, A., Corbett, B. C., Corbett, J., Cordier, P., Cremon, M. A., Crook, C. M., Cusini, M., Fei, F., Frambati, S., Franc, J., Franceschini, A., Frigo, M., . . . Wu, H. (2024). GEOS: A performance portable multi-physics simulation framework for subsurface applications. *Journal of Open Source Software*, *9*(102). https://doi.org/10.21105/joss.06973

Shreedharan, S., Rivière, J., Bhattacharya, P., & Marone, C. (2019). Frictional State Evolution During Normal Stress Perturbations Probed With Ultrasonic Waves. *Journal of Geophysical Research: Solid Earth*, *124*(6), 5469-5491. https://doi.org/10.1029/2018jb016885

Wang, C., Eaton, D. W., & Ma, Y. (2023). Numerical modeling of low-frequency distributed acoustic sensing signals for mixed-mode reactivation. *Geophysics*, *88*(6), WC25–WC36.